

COMPUTATIONAL ASPECTS OF DIFFUSE OPTICAL TOMOGRAPHY

Diffuse optical tomography (DOT) is a novel functional imaging modality for visualizing and continuously monitoring tissue and blood oxygenation levels, which is useful for brain imaging and tumor detection. Because of the nonlinearity of infrared light propagation in tissue, developing fast and robust reconstruction methods is the main challenge in making DOT a viable tool for clinical diagnostics.

Volume images of the body are an indispensable clinical diagnostic tool. For visualizing and examining complex body organs such as the brain, doctors depend on the information 3D imaging modalities, such as x-ray computed tomography (CT) and magnetic resonance imaging (MRI), provide. Although these mature techniques have developed into reliable systems delivering high-quality images, some drawbacks remain. MRI requires a large and expensive instrument with considerable maintenance costs, while CT uses ionizing radiation, which is potentially harmful to patients. Today, the drive is toward relatively inexpensive, noninvasive, and portable imaging systems that can run at a patient's bedside and produce data continuously over a long period of time.

Although CT and MRI provide primarily anatomical information about tissue structure, interest is shifting toward functional imaging modalities that provide information about physiologically relevant parameters and parameter

changes (tissue oxygenation level, for example) and can be used in applications like brain activation monitoring.

Diffuse optical tomography (DOT) can potentially meet these criteria. Like CT, it uses electromagnetic radiation to probe the body, but at a much lower energy level and therefore doesn't damage tissue. DOT operates at wavelengths at the red end of the visible spectrum and in the near-infrared range, around 650 to 900 nanometers. This spectral range is called a *window of transparency* because it lets light propagate relatively deeply into the tissue before being absorbed. At longer wavelengths the absorption spectrum of water rises steeply, whereas toward lower wavelengths, blood becomes a strong absorber, essentially blocking all light transmission within a few millimeters. Researchers have known for several decades that light can propagate through thick sections of body organs.¹ The exciting feature of infrared light is that its absorption by blood and tissue depends on their oxygenation state,² which lets us directly measure the body's oxygenation levels. Spectroscopic applications such as pulse oximetry,³ which clinicians routinely use, exploit this feature. The use of infrared light in tomographic imaging makes DOT a functional imaging modality with potentially significant applications in brain function imaging and early tumor detection. (See articles by David Boas and colleagues⁴ and Arjun Yodh and Britton

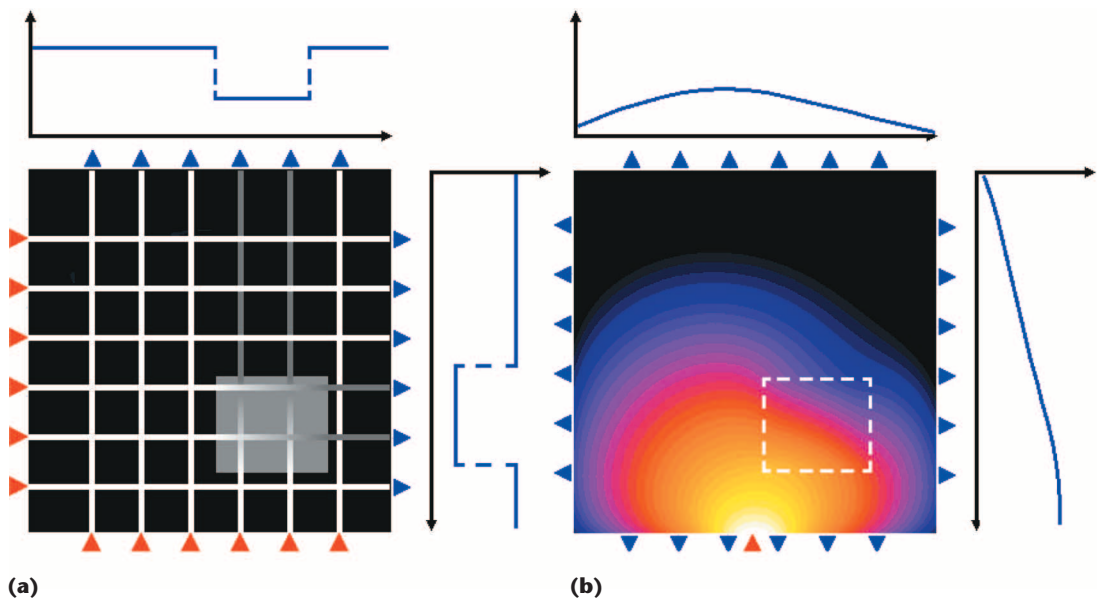


Figure 1. Diffuse light transport. (a) A schematic view of computed tomography (CT)-like projections along straight lines, where included objects cast “shadows” on the opposite detector array. (b) Photon density wave from a single source propagating through a diffuse medium with an embedded object. Detectors placed around the surface maximize data information.

Chance⁵ for reviews of DOT methodology and current applications.)

Diffuse Light Transport

The use of infrared light for imaging presents a big challenge: Unlike the radiation in CT, which generally travels in straight lines through the body, infrared light is strongly scattered by tissue. For most tissue types, a photon’s mean free path of travel between two scattering events is only a fraction of a millimeter. Therefore, any photons that penetrate the tissue will have undergone multiple scattering events. Instead of a pencil beam of radiation traveling through tissue, we face a diffuse photon density wave. In the high-scattering regime, we can consider light as a stream of particles (photons) and the photon density wave as the spatial and temporal distribution of the density of photons in the scattering medium. Figure 1a shows a schematic view of the straight-line projections encountered in CT imaging, and Figure 1b shows a photon density field calculated for a scattering medium with an embedded rectangular object.

Diffuse light propagation complicates image reconstruction. Light traveling between two points on the surface spreads out over a significant volume inside the tissue and therefore carries very little spatial information. To maximize the information contained in the measurements, we use multiple

detectors to sample the light emerging over a large surface area from the body for each source. The problem now is to reconstruct images of the internal distribution of the tissue’s optical properties from these boundary measurements. Unlike CT, this problem is highly nonlinear, and analytical solutions exist only for a limited number of geometries.⁶ In general, we must resort to an iterative approach, which we state as

Given a model of diffuse light transport in scattering media that calculates boundary measurement data for a given set of volume optical parameters, find a set of parameters that will minimize the difference between the measured and the model data.

We choose the diffusion equation as our model of diffuse light propagation. This model works well when scattering is stronger than absorption, which is generally true for biological tissue, and when we can neglect anisotropic effects. More sophisticated models can be used⁷ if these assumptions do not hold—for example, in low-scattering regions, such as the cerebrospinal fluid (CSF), or regions with directional preferences, such as nerve bundles.

Because we have no analytical solutions to the diffusion equation for general inhomogeneous problems, we use a finite-element model (FEM) to

obtain numerical solutions. Our FEM implementation for DOT uses a range of element types such as isoparametric and subparametric tetrahedra or regular voxel grids, and supports sparse direct or preconditioned iterative linear solvers. Because we can distribute individual input source computations with minimal data exchange, FEM in DOT reconstruction problems is trivially suited for parallel processing.

The diffusion equation expresses the photon density field as a function of parameters μ_a (the absorption coefficient) and μ'_s (the transport-scattering coefficient). Both parameters are generally unknown, so the reconstruction algorithm must recover them simultaneously. A common difficulty in DOT is the occurrence of cross-talk between the absorption and scattering images—that is, absorption features might produce image artifacts in the scattering image, and vice versa.

Data type selection significantly affects the ability to distinguish absorption and scattering properties.⁸ The measurement of intensity transmitted through the tissue from a continuous wave source yields a poor separation between the parameters. Most DOT data acquisition systems therefore use time-of-flight setups to measure the temporal dispersion of light from an ultrashort incident pulse^{9,10} or frequency-domain systems, which measure the complex transmission intensity at one or several modulation frequencies.¹¹ In this article, we consider data from a frequency-domain system. In practice, such systems usually measure the transmitted signal's modulation amplitude and phase shift.

Photon Measurement Density Functions

Many image reconstruction algorithms require calculating the measurement operator's derivative with respect to the optical parameters $\partial y_i / \partial (\mu_a)_j$ and $\partial y_i / \partial (\mu'_s)_j$ for a measurement $y_i = f_i[\mu_a(r), \mu'_s(r)]$ and a pixel j of the image. For each measurement i , these derivatives form a spatial map of the measurement's sensitivity to a perturbation of the optical parameters at each image point. These sensitivity maps, or photon measurement density functions (PMDF), show the volume of tissue probed by a given measurement and indicate the spatial information contained in that measurement. Figure 2a shows the absorption sensitivity regions for two boundary modulation amplitude measurements. The PMDF is negative everywhere, indicating that increased absorption causes the modulation amplitude to decrease. Measurement sensitivity is highest in the areas directly under the source and detector sites,

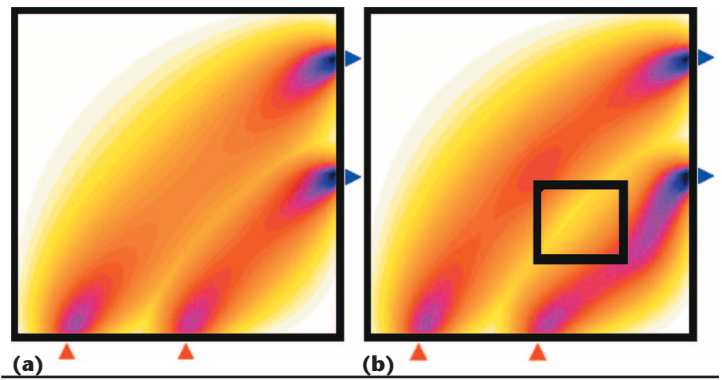


Figure 2. Measurement sensitivity region perturbation by internal optical parameters' inhomogeneity. (a) Sensitivity map containing two measurements of modulation amplitude against a perturbation for a homogeneous case, and (b) the same map distorted by the presence of a rectangular object of increased absorption and scattering.

dropping toward the domain's interior.

We now place a rectangular object of increased absorption and scattering into the homogeneous background. Figure 2b shows how the inclusion affects the PMDFs' shape. The sensitivity regions are bent away from the inclusion, indicating that light must travel around the high-contrast object to be registered by the detector.

The PMDFs' dependency on the volume optical parameter distribution, which demonstrates the imaging problem's nonlinearity, profoundly affects image reconstruction algorithms, which use PMDFs to back-project measurement differences into the interior to form an image. Because we update the $\mu_a^{(k)}$ and $\mu'_s^{(k)}$ estimates at each iteration k , we must also recalculate the PMDF at each iteration to reflect the changes.

Image Reconstruction

Reconstruction in DOT is almost always a nonlinear problem—that is, the relationship between a change in the volume tissue parameters and the resulting changes in the boundary data is nonlinear. In certain simple circumstances, such as a change in a point-like perturbation included in a homogeneous medium, linear methods might be applicable, but these cases are of little significance in clinical applications.

We implement the image reconstruction scheme as an optimization problem by defining an objective function that describes the difference between the vector of measurement data M_i and the vector of boundary projections calculated with the light transport model for a given set of parameters $f_i[\mu_a, \mu'_s]$. We use a weighted L_2 norm to define our objective function $\psi = \sum_i (f_i[\mu_a, \mu'_s] - M_i)^2 \sigma_i^{-2}$, where

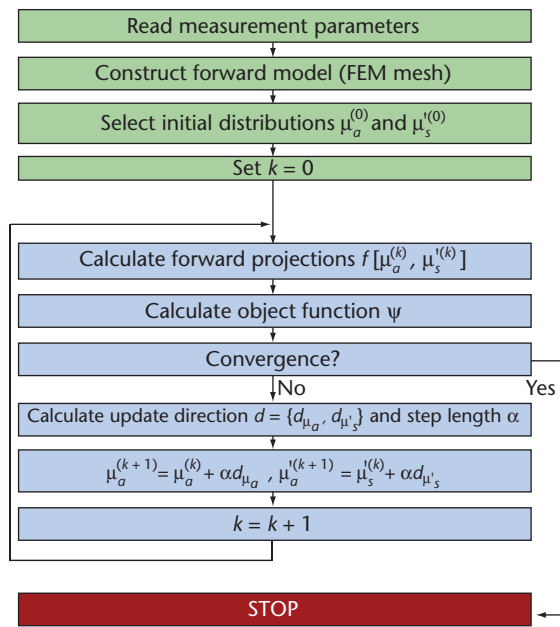


Figure 3. Schematic flow of iterative nonlinear reconstruction procedure.

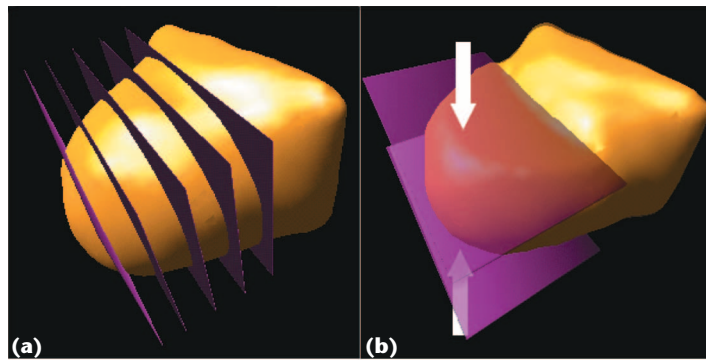


Figure 4. Breast mesh for two measurement arrangements: (a) unconstrained mesh, in which sources and detectors are arranged in five planes on the surface; and (b) mesh compressed by parallel plates to a thickness of 6 cm, where the source scans across the top plate, and the detector scans across the bottom.

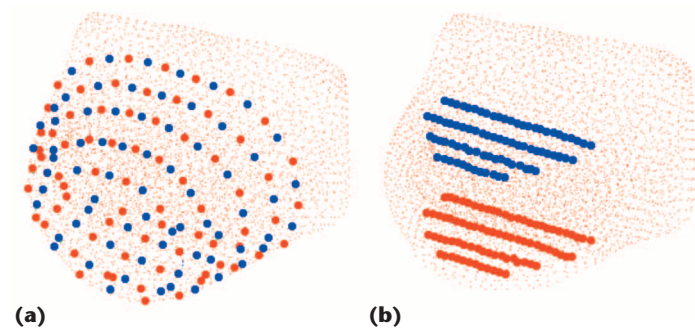


Figure 5. Source and detector arrangement for the breast imaging problems for (a) unconstrained and (b) compressed cases. Source positions are in blue, detector positions in red.

σ_i is an estimate of the standard deviation for measurement i . Figure 3 shows a schematic flow diagram for the iterative inverse solver. At the heart of the program is the calculation of updates $\Delta \mu_a = \alpha d_{\mu_a}$ and $\Delta \mu_s = \alpha d_{\mu_s}$, which we obtain using a gradient-based method, such as nonlinear conjugate gradients, or a Newton-type solver.

Breast Imaging

Optical mammography could be used to detect breast cancer at an early stage. Unlike x-ray mammography, which detects microcalcifications characteristic of malignant lesions, optical mammography senses changes in blood perfusion of the tissue surrounding the tumor. These changes occur early in a tumor's growth and can affect a relatively large area, so spatial resolution is less critical in optical methods.

Several instrumentation types exist for optical mammography. In one, parallel plates, similar to the setup in x-ray mammography, compress the breast. A laser source then scans across one of the transparent plates, while a detector on the opposite plate scans over several measurement locations for each source position. This arrangement reduces the thickness of the transilluminated tissue, improving the detectability of deeply embedded objects. The compression can cause blood to drain from the breast, however, unpredictably altering the optical properties. Furthermore, projection angle limitations inherent in the method can result in image degradation.

In an alternative arrangement, the patient lies prone on a table with the unsupported breast suspended in a cavity. The data acquisition system might consist of a set of fixed sources and detectors or a rotating system that scans the breast's surface. This setup can provide a more complete sampling of data over the boundary, but makes defining the problem's geometry more difficult. In this article, we present reconstruction results from both setups.

We constructed a mesh consisting of 4,756 nodes and 21,723 tetrahedral elements from a segmented 3D MRI image of an unsupported breast. The mesh defines internal regions of adipose and fibrous tissue, as well as a cancerous lesion. Figure 4a shows the mesh surface. The image also indicates the measurement planes on which the source and detector sites are located.

To obtain the modified mesh for the compression case, we applied an FEM for linear elastic deformation.¹² We compressed the front part of the breast to a thickness of 6 cm; Figure 4b shows the resulting mesh's surface. For this case we assume the source scans across the top compression sur-

face, and the detector across the bottom surface.

Figure 5 shows the arrangement of source and detector sites for both cases. Figure 5a shows the unconstrained case, with 72 sources and 72 detectors arranged in five rings. Figure 5b shows the compressed case, with 81 sources in four lines along the top surface, and 81 detectors arranged in four lines along the bottom surface. In each case, we illuminate the sources sequentially and for each source record measurements at all detector locations. Each measurement consists of the modulation amplitude and phase shift for an input signal modulated at 50 MHz.

Figures 6 and 7 show the reconstruction results of the unconstrained and the compressed mesh problems. We performed the reconstructions from two starting distributions $\mu_a^{(0)}$ and $\mu_s^{(0)}$. In the first case, we assume no prior knowledge of the optical properties' internal distribution, and start from a homogeneous parameter distribution. In the second case, we start from the background image containing the fibrous tissue distribution, assuming a known internal structure—for example, from a previously acquired image—but assume no information about the tumor's existence. In all cases, the reconstruction algorithm localizes the tumor; however, the spatial resolution and contrast improve significantly when the background tissue's internal structure is known, demonstrating the importance of incorporating prior knowledge into reconstruction.

The compressed mesh reconstructions show a lower resolution in the vertical direction perpendicular to the compression plates. This effect is due to the limitation in measurement projection angles. To solve this problem, we could acquire two separate images in which the breast is compressed in two directions.

A detailed description of the mathematical background, which is beyond this article's scope, is available elsewhere.¹³

Brain Imaging

Optical tomography of the brain has a range of applications. Physicians can use it to measure blood and tissue oxygenation locally to detect early stages of oxygen deficiency in newborn and preterm babies, a common cause of death and permanent brain damage. DOT is also effective in functional brain activation imaging, because active areas of the brain show local changes in oxygen delivery and uptake, which optical measurements can detect. Other applications include studying brain development and monitoring the effect of treatment. Jeremy C. Hebden and colleagues recently pre-

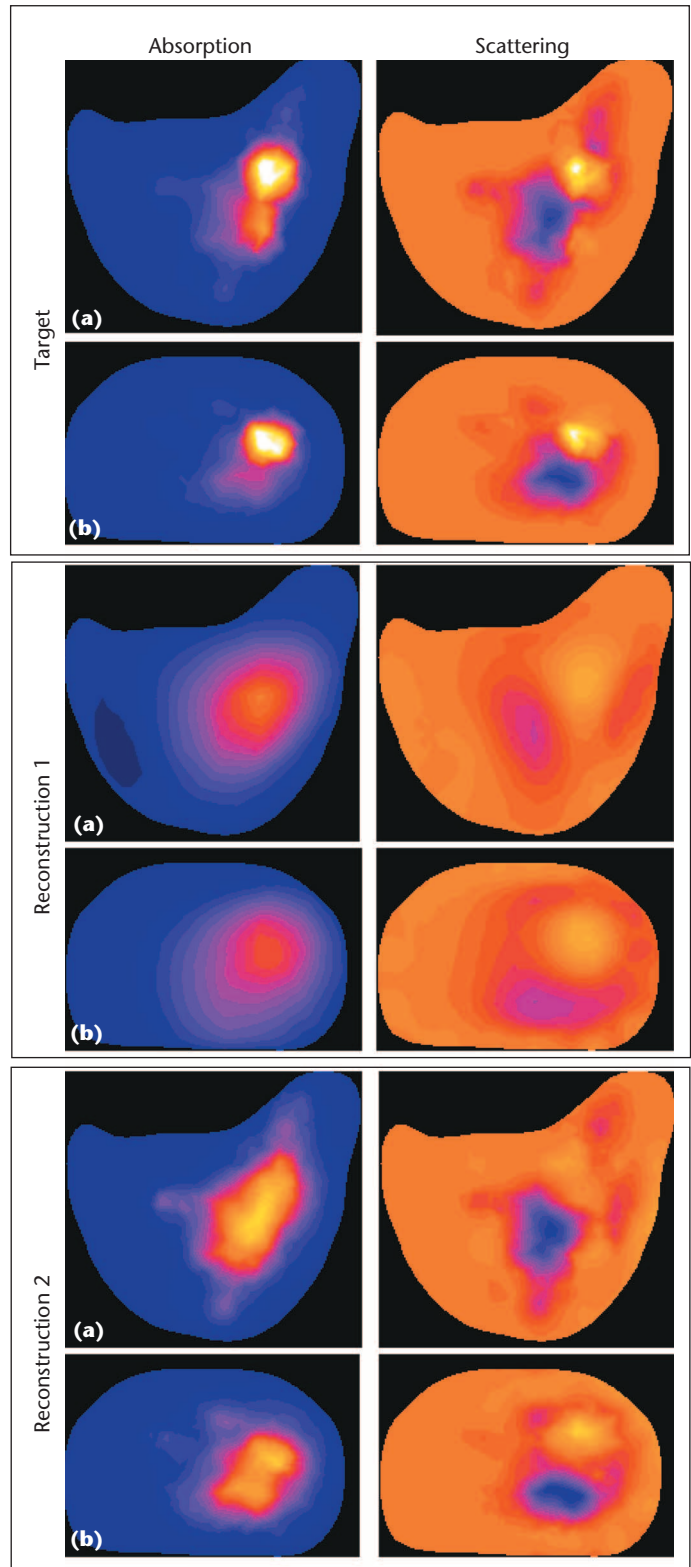


Figure 6. Reconstruction results for unconstrained breast mesh. Two cross sections, (a) unconstrained and (b) compressed, show absorption and scattering images for target, reconstruction 1 starting from a homogeneous background, and reconstruction 2 starting from correct background. Color ranges are $0.006 \text{ mm}^{-1} \leq \mu_a \leq 0.015 \text{ mm}^{-1}$ and $0.8 \text{ mm}^{-1} \leq \mu_s \leq 1.16 \text{ mm}^{-1}$.

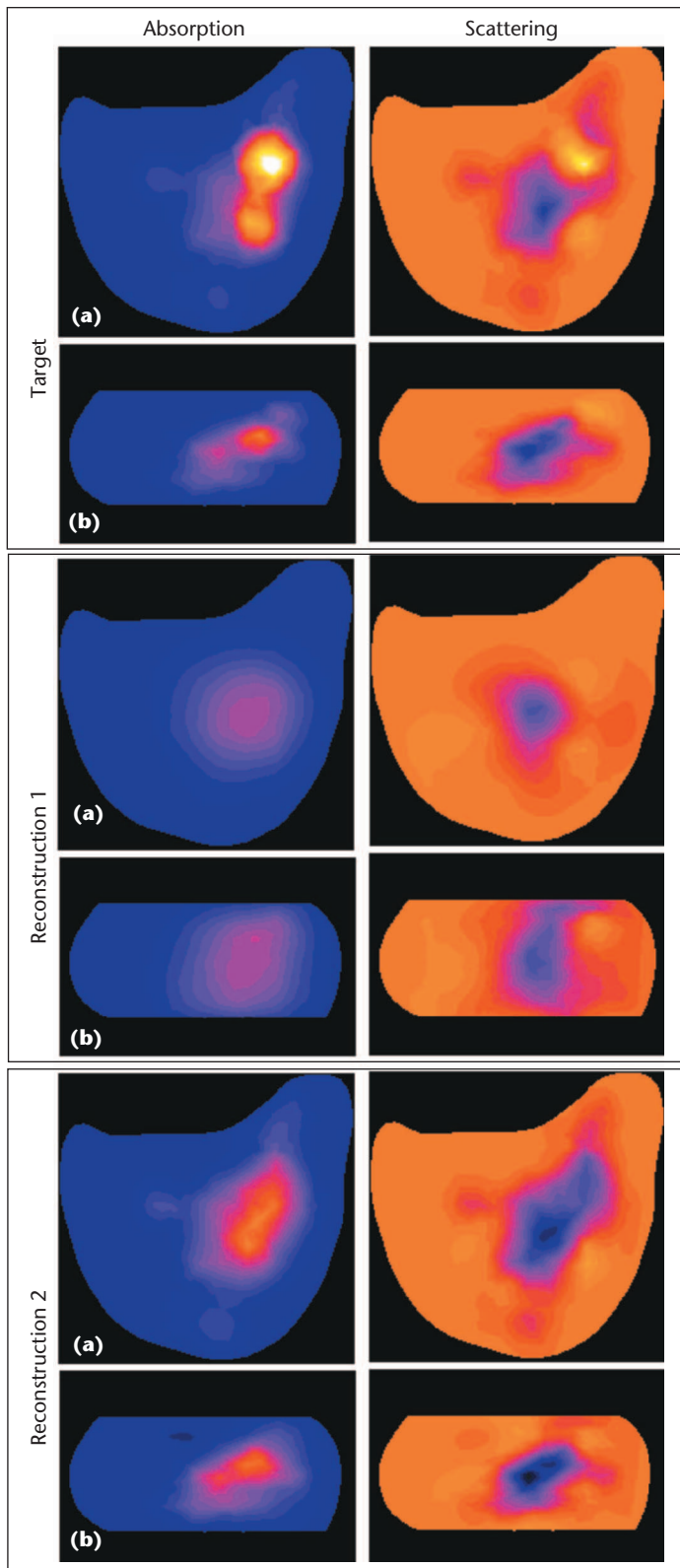


Figure 7. Reconstruction results for compressed breast mesh. Two cross sections, (a) unconstrained and (b) compressed, show absorption and scattering images for target, reconstruction 1 starting from a homogeneous background, and reconstruction 2 starting from correct background. Color ranges are as in Figure 6.

sented images reconstructed from data obtained on premature infants.¹⁴

Because of its complexity, the head is more challenging for image reconstruction in DOT than the breast. Light must penetrate the skin and skull before reaching the brain tissue we want to image. The brain floats in the CSF, a clear liquid that can significantly affect light propagation. Finally, the brain's white matter consists of bundles of aligned nerve fibers, which cause anisotropic radiation transport.

Our first objective was to construct a finite-element mesh for the light transport model. We generated a mesh based on a 3D MRI image. Figure 8 shows a cross section of this mesh. Meshing complex objects with a high level of detail in the internal structure is a nontrivial problem. We adopted a straightforward approach, converting the MRI image directly into a structured mesh built from regular voxel elements after downsampling the image to a suitable resolution. We map μ_a and μ_s' from the MRI image's gray levels using a mapping function based on known optical parameters for different tissue types. Figure 9 shows the absorption and scattering distributions on cross sections of the resulting images. To simulate the effect of an anomalous region, such as a lesion or localized perfusion change, we placed spherical absorption and scattering test objects in the anterior and posterior regions of the brain, respectively. White circles represent these objects in the images.

Figure 10 shows the voxel mesh surfaces for voxel resolutions of $128 \times 128 \times 80$ and $32 \times 32 \times 20$. Although the regular voxel grid produces a ragged surface, which is particularly apparent at lower resolutions, using a regular grid has advantages for the FEM forward solver in terms of memory efficiency and convergence rate: The elements' invariant shape avoids the need to store geometric parameters for individual elements and leads to better conditioned FEM system matrices. To improve the representation of smooth surfaces, we could adapt a hybrid mesh approach by padding the boundary layer with unstructured tetrahedral elements.

Figure 10 also shows the location of the three measurement planes along which we've arranged the sources and detectors of the simulated data acquisition system. We use a measurement geometry with 16 sources and 16 detectors in the central plane, and eight sources and eight detectors in the top and bottom planes. We generate phase shift and modulation-amplitude data at an input modulation frequency of 50 MHz at all detector sites, in-

cluding cross-plane measurements, yielding 1,024 measurements. Figure 11 shows source and detector placement on the mesh surface.

Figure 12 shows our reconstructions results. We reconstructed absorption and scattering images into a $12 \times 12 \times 12$ trilinear voxel basis, starting from either homogeneous background values (Figure 12a) of $\mu_a = 0.023 \text{ mm}^{-1}$ and $\mu_s' = 0.9 \text{ mm}^{-1}$, which represent average values for the background parameters, or the background parameter distribution without the inclusions (Figure 12b). We used the coarse $32 \times 32 \times 20$ voxel mesh shown in Figure 10b to drive the FEM forward model. Both the absorption and scattering features are localized correctly. The recovered images' spatial resolution is relatively low, owing to the coarseness of the inverse basis representation. The low resolution of the solution basis constitutes an implicit regularization by suppressing high spatial frequencies in the reconstructed images. Using a higher resolution basis reduces the solver's convergence rate and can lead to high-frequency artifacts in the image, making it undesirable for this problem.

In this simplistic reconstruction problem we've neglected the effects of low scattering in the CSF layer and anisotropy of the brain tissue. Simon R. Arridge and colleagues present a more sophisticated hybrid model of light transport that uses a radiosity method to solve the propagation problem in nonscattering regions.¹⁵

Image reconstruction methods that account for the reconstruction problem's nonlinearity might provide imaging tools that allow a fully 3D simultaneous reconstruction of absorption and scattering images. Guaranteeing a satisfactory correspondence with experimental data will require improving the light transport model. In particular, in brain imaging, the presence of low-scattering areas (CSF) and anisotropic scattering in regions with aligned nerve fiber bundles might necessitate the use of more sophisticated radiative transport models.

Several research groups are currently developing prototype optical tomography systems^{14,16} and testing them in clinical brain- and breast-imaging trials. Some commercial instruments (dynamic near infrared optical tomography [DYNOT] by NIRx Medical Technologies, computed tomography laser breast imaging [CTLM] by Imaging Diagnostic Systems, and SoftScan by Advanced Research and Technologies) are already available or

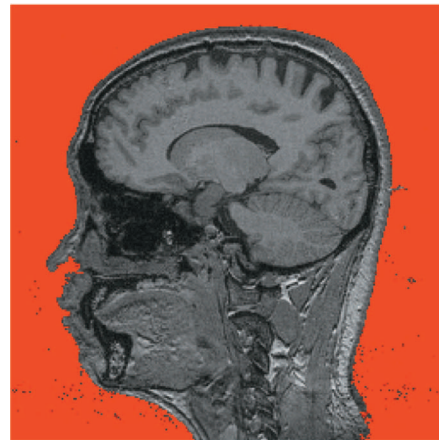


Figure 8. Sagittal cross section of a $256 \times 256 \times 160$ MRI image after boundary detection (exterior pixels marked red), and before eliminating mislabeled voxels.

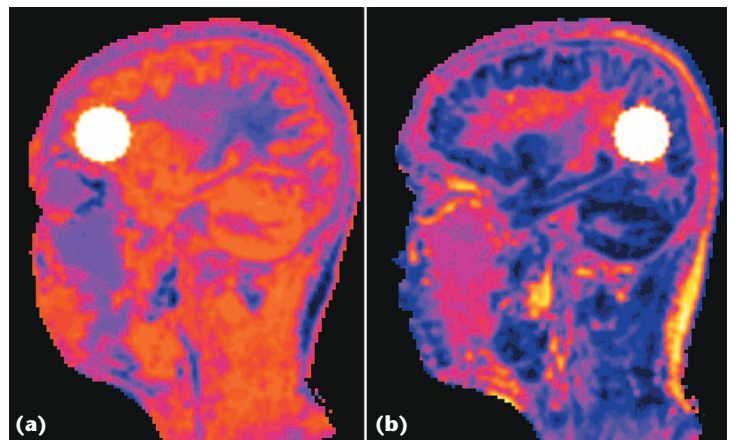


Figure 9. (a) Absorption and (b) scattering target image cross section mapped from the MRI gray-level image.

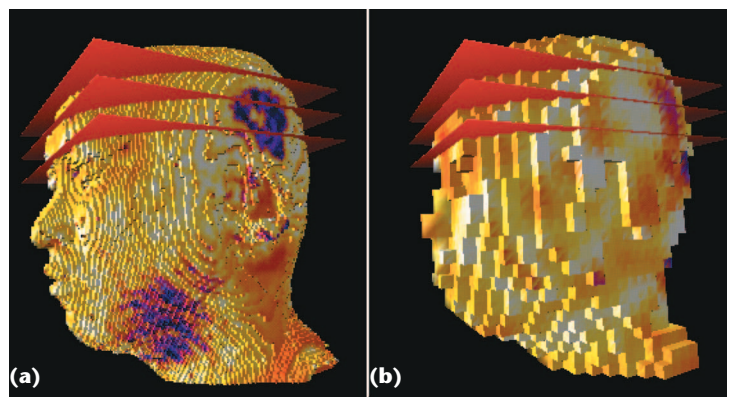


Figure 10. Surface of voxel head mesh at resolution (a) $128 \times 128 \times 80$ and (b) $32 \times 32 \times 20$ generated from downsampled MRI 3D volume image. Orange planes indicate the measurement planes containing source and detector sites.

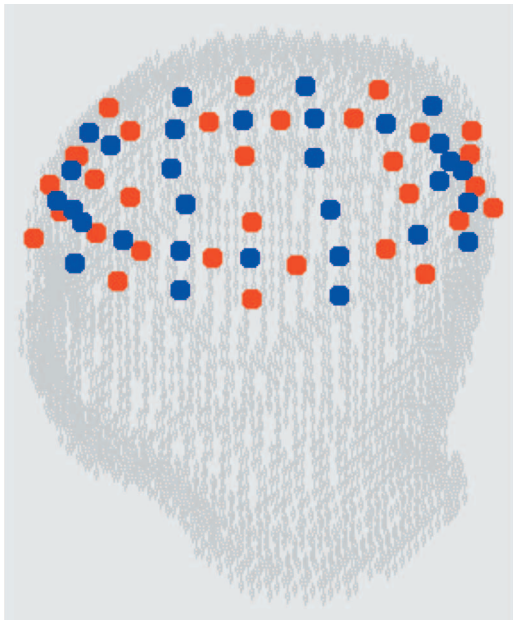


Figure 11. Source and detector placements in three rings for data acquisition on the head model.

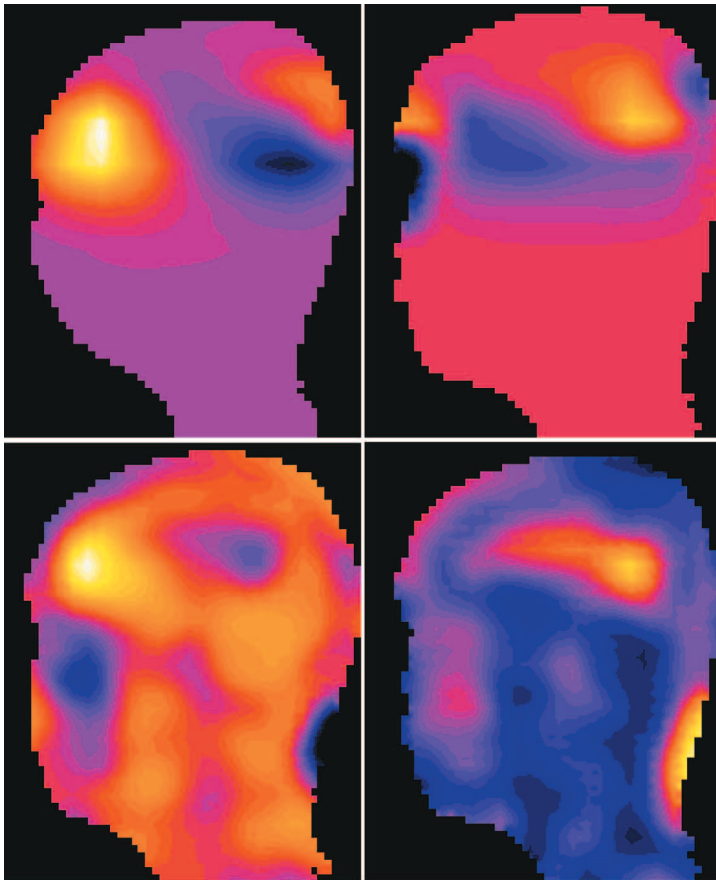


Figure 12. Cross sections of the reconstructed (left) absorption and (right) scattering distributions of the head model from homogeneous background parameters and known background parameters.

awaiting FDA approval. With the emergence of fast data-acquisition systems, and simultaneous work done on reconstruction algorithms, clinical systems should make their way into diagnostic practice within the next decade. We can expect the first systems to be used in the two main fields of optical mammography and brain oxygenation monitoring of newborn infants. A promising future path for optical tomography is the fusion with other, high-resolution modalities which provide a priori structural information to guide the reconstruction process in DOT.

Acknowledgments

This work was supported by the Engineering and Physical Sciences Research Council-Medical Research Council Interdisciplinary Research Consortium (EPSRC-MRC IRC) program, "From Medical Images and Signals to Clinical Information."

We thank Chloe Hutton, the Institute of Neurology, London, and Atsushi Maki, Hitachi, Japan, for their help in preparing the 3D MRI head images, and Christine Tanner, King's College London, for providing the breast meshes presented in this article.

The finite-element software package used to generate the images presented in this article is publicly available at www.medphys.ucl.ac.uk/~martins/toast/index.html.

References

1. J.J. Jöbsis, "Noninvasive Infrared Monitoring of Cerebral and Myocardial Oxygen Sufficiency and Circulatory Parameters," *Science*, vol. 198, Dec. 1977, pp. 1264–1267.
2. S. Takatani and M.D. Graham, "Theoretical Analysis of Diffuse Reflectance from a Two-Layer Tissue Model," *IEEE Trans. Biomedical Eng.*, vol. 26, no. 12, 1979, pp. 656–664.
3. M. Schmitt, "Simple Photon Diffusion Analysis of the Effects of Multiple Scattering on Pulse Oximetry," *IEEE Trans. Biomedical Eng.*, vol. 38, no. 12, 1991, pp. 1194–1203.
4. D.A. Boas et al., "Imaging the Body with Diffuse Optical Tomography," *IEEE Signal Processing*, vol. 18, no. 6, 2001, pp. 57–75.
5. A. Yodh and B. Chance, "Spectroscopy and Imaging in Diffusing Light," *Physics Today*, vol. 48, no. 3, 1995, pp. 34–40.
6. V.A. Markel and J.C. Schotland, "Inverse Problem in Optical Diffusion Tomography, I. Fourier Laplace Inversion Formulas," *J. Optical Soc. Am. A*, vol. 18, no. 6, 2001, pp. 1336–1347.
7. O. Dorn, "A Transport-Backtransport Method for Optical Tomography," *Inverse Problems*, vol. 14, no. 5, 1998, pp. 1107–1130.
8. M. Schweiger and S.R. Arridge, "Optimal Data Types in Optical Tomography," *Proc. Information Processing in Medical Imaging (IPMI 97)*, LNCS 1230, Springer, 1997, pp. 71–84.
9. J.C. Hebden, S.R. Arridge, and D.T. Delpy, "Optical Imaging in Medicine: I. Experimental Techniques," *Physics in Medicine and Biology*, vol. 42, no. 5, 1997, pp. 825–840.
10. D. Grosenick, H. Wabnitz, and H. Rinneberg, "Time-Resolved Imaging of Solid Phantoms for Optical Mammography," *Applied Optics*, vol. 36, no. 1, 1997, pp. 221–231.

ADVERTISER / PRODUCT INDEX

November / December 2003

11. B.W. Pogue and M.S. Patterson, "Frequency-Domain Optical Absorption Spectroscopy of Finite Tissue Volumes Using Diffusion Theory," *Physics in Medicine and Biology*, vol. 39, 1994, pp. 1157-1180.
12. O.C. Zienkiewicz and R.L. Taylor, *The Finite Element Method*, 4th ed., McGraw-Hill, 1987.
13. S.R. Arridge, "Optical Tomography in Medical Imaging," *Inverse Problems*, vol. 15, no. 2, Apr. 1999, pp. R41-R92.
14. J.C. Hebden et al., "Three-Dimensional Optical Tomography of the Premature Infant Brain," *Physics in Medicine and Biology*, vol. 47, no. 23, Dec. 2002, pp. 4155-4166.
15. S.R. Arridge et al., "The Finite Element Method for the Propagation of Light in Scattering Media: A Direct Method for Domains with Nonscattering Regions," *Medical Physics*, vol. 27, no. 1, 2000, pp. 252-264.
16. A.M. Siegel, J.J.A. Marota, and D.A. Boas, "Design and Evaluation of a Continuous-Wave Diffuse Optical Tomography System," *Optics Express*, vol. 4, no. 8, 1999, pp. 287-298.

Martin Schweiger is a senior research fellow in the Department of Computer Science, University College London, UK. His research interests include numerical modeling, finite elements, inverse problems, and medical imaging. He has a diploma in physics from Ludwig-Maximilian University Munich, Germany, and a doctorate in medical physics from University College London. Contact him at M.Schweiger@cs.ucl.ac.uk.

Adam Gibson is a research fellow with the Department of Medical Physics and Bio-engineering at University College London. His research interests are in medical imaging, particularly brain imaging using optical and electrical impedance tomography. He has a PhD in medical physics from UCL. He is a member of the Institute of Physics. Contact him at agibson@medphys.ucl.ac.uk.

Simon R. Arridge is a professor in the Department of Computer Science at University College London. His research interests include inverse problems, computational methods in medical imaging, and numerical modeling. He has a BA in natural sciences from Cambridge University and a PhD in medical physics from UCL. He is a member of the Institute of Physics and the Engineering and Physical Sciences Research Council College. Contact him at s.arridge@cs.ucl.ac.uk.

Advertisers	Page Number
Ciphergen	14
John Wiley & Sons, Inc.	Inside front cover
Krell Institute	9, 12
Preclinical Development Forum	Inside back cover
Sandia National Laboratories	5

Advertising Personnel

Marion Delaney IEEE Media, Advertising Director Phone: +1 212 419 7766 Fax: +1 212 419 7589 Email: md.ieeemedia@ieee.org	Sandy Brown IEEE Computer Society, Business Development Manager Phone: +1 714 821 8380 Fax: +1 714 821 4010 Email: sb.ieeemedia@ieee.org
Marian Anderson Advertising Coordinator Phone: +1 714 821 8380 Fax: +1 714 821 4010 Email: manderson@computer.org	

Advertising Sales Representatives

Mid Atlantic (product/recruitment) Dawn Becker Phone: +1 732 772 0160 Fax: +1 732 772 0161 Email: db.ieeemedia@ieee.org	Midwest/Southern (recruitment) Darcy Giovingo Phone: +1 847 498-4520 Fax: +1 847 498-5911 Email: dg.ieeemedia@ieee.org	Southern CA (product) Marshall Rubin Phone: +1 818 888 2407 Fax: +1 818 888 4907 Email: mr.ieeemedia@ieee.org
New England (product) Jody Estabrook Phone: +1 978 244 0192 Fax: +1 978 244 0103 Email: je.ieeemedia@ieee.org	Midwest (product) Dave Jones Phone: +1 708 442 5633 Fax: +1 708 442 7620 Email: dj.ieeemedia@ieee.org	Northwest/Southern CA (recruitment) Tim Matteson Phone: +1 310 836 4064 Fax: +1 310 836 4067 Email: tm.ieeemedia@ieee.org
New England (recruitment) Barbara Lynch Phone: +1 401 739-7798 Fax: +1 401 739 7970 Email: bl.ieeemedia@ieee.org	Will Hamilton Phone: +1 269 381 2156 Fax: +1 269 381 2556 Email: wh.ieeemedia@ieee.org	Japan (product/recruitment) German Tajiri Phone: +81 42 501 9551 Fax: +81 42 501 9552 Email: gt.ieeemedia@ieee.org
Connecticut (product) Stan Greenfield Phone: +1 203 938 2418 Fax: +1 203 938 3211 Email: greenco@optonline.net	Joe DiNardo Phone: +1 440 248 2456 Fax: +1 440 248 2594 Email: jd.ieeemedia@ieee.org	Europe (product) Hilary Turnbull Phone: +44 131 660 6605 Fax: +44 131 660 6989 Email: impress@impressmedia.com
Southeast (product/recruitment) C. William Bentz III Email: bb.ieeemedia@ieee.org Gregory Maddock Email: gm.ieeemedia@ieee.org Sarah K. Wiley Email: sh.ieeemedia@ieee.org Phone: +1 404 256 3800 Fax: +1 404 255 7942	Southwest (product) Bill Wageneck Phone: +1 972 423 5507 Fax: +1 972 423 6858 Email: bill.wageneck@wageneck-associates.com	Europe (recruitment) Penny Lee Phone: +20 7405 7577 Fax: +20 7405 7506 Email: reception@essential-media.co.uk
	Northwest (product) Peter D. Scott Phone: +1 415 421-7950 Fax: +1 415 398-4156 Email: peterd@pscottassoc.com	

Computing in Science & Engineering

IEEE Computer Society
 10662 Los Vaqueros Circle
 Los Alamitos, California 90720-1314
 USA
 Phone: +1 714 821 8380
 Fax: +1 714 821 4010
<http://computer.org>
advertising@computer.org